Title

Hydromechanical reactivation of natural discontinuities: mesoscale experimental observations and DEM modeling

Journal

Acta Geotechnica, 14(5)

ISSN

1861-1125

Authors

Tsopela, Alexandra
Donzé, Frédéric-Victor
Guglielmi, Yves
et al.

Publication Date

2019-10-01

DOI

10.1007/s11440-019-00791-0

Peer reviewed

Hydromechanical reactivation of natural discontinuities: mesoscale experimental observations and DEM modeling

Alexandra Tsopela[1] • Frederic-Victor Donze[1] • Yves Guglielmi[2] • Raymi Castilla3 • Claude Gout[3]

[1] Univ. Grenoble Alpes, Univ. Savoie Mont Blanc, CNRS, IRD, IFSTTAR, ISTerre, 38000 Grenoble, France [2] Earth and Environmental Science Area, Lawrence Berkeley National Laboratory, Berkeley, CA 94720, USA [3] Total, Jean Feger Scientific and Technical Center, Avenue Larribau, 64018 Pau, France

Abstract

Fracture interaction mechanisms and reactivation of natural discontinuities under fluid pressurization conditions can represent critical issues in risk assessment of caprock integrity. A field injection test, carried out in a damage fault zone at the decameter scale, i.e., mesoscale, has been studied using a distinct element model. Given the complex structural nature of the damage fault zone hydraulically loaded, the contribution of fracture sets on the bulk permeability has been investigated. It has been shown that their orientation for a given in situ stress field plays a major role. Based on these results, a simpler model with a fluid-driven fracture intersecting a second fracture has been set up to perform a sensitivity analysis. It is in presence of a minimum differential stress value with a minimum angle with the maximum principal stress that the second fracture could be both, hydraulically and mechanically reactivated. Results also showed that in the vicinity of the fluid-driven fracture, a natural fracture will offer contrasted hydromechanical responses on each side of the intersection depending on the stress conditions and its orientation with respect to the stress field. In this case, we show that a hydromechanical decoupling can occur along the same plane. These results provide insights into fracture-controlled permeability of fault zones depending on the properties of the fractures and their hydromechanical interactions for a given in situ stress field.

Keywords

Caprock integrity, Distinct element method model, Fracture interaction, Natural fracture reactivation

1 Introduction

The reactivation of natural discontinuities under pressurized fluid conditions can become highly critical when considering geo-storage of pressurized supercritical gas like carbon dioxide, methane or dihydrogen. This represents a major concern to control the long-term retention of fluids in subsurface reservoirs [44, 58]. These preexisting fracture sets can be a part of bedding plane or inherited joint systems as well as fault zones [16, 44, 55, 58]. Depending on the in situ stress context, these connected fractures can significantly increase the permeability, providing drains on long distance in

the presence of mature faults [42, 45]. In many cases, fault permeability is accepted to be fracture dominated [3, 48] as the high-permeability damage zone can provide a potential fracture flow network especially in low-porosity rocks. When considering the fracture-controlled permeability, one must account for complex hydromechanical mechanisms occurring upon the reactivation even at the single fracture scale [2, 6, 17, 27, 31, 39]. However, in situ hydromechanical coupled effects within one fracture depend not solely on its own properties, but also on the nature of the hydromechanical connections with other fractures, the distribution, the size and the orientation of these neighboring fractures, their aperture distribution, their orientation and the magnitude of effective stresses applied [7, 12, 41]. It is generally accepted that critically stressed structures are hydraulically conductive [4, 5, 52]. In natural conditions, the reactivation of a natural fracture hydraulically connected with a fluid-pressurized fracture can be quite complex.

Based on laboratory tests investigating the interaction between a fluid-driven fracture and a natural fracture [26, 55, 62], three types of interactions are reported. Depending on various parameters, (1) the hydraulic fracture can cross the natural fracture, (2) it can be stopped by the natural fracture, or (3) it hydraulically activates the natural fracture. Microseismic imaging of hydromechanical reactivation of fractures is a useful tool to assess fracture geometry, i.e., the fracture height, length, orientation [40], frictional properties [23], and fractures interaction [47, 54, 56]. However, the interpretation of the induced microseismicity is not straightforward since pore pressure perturbations can promote both seismic and aseismic motions [14] with the induced slip not necessarily being the source of instability [35]. Indeed, well-monitored recent in situ hydromechanical tests in fault zones show that an important part of the deformation induced by injection is aseismic [19, 22, 29]. To better capture and understand aseismic deformation, fracture interaction, and the associated permeability increase that can hardly be quantified from seismic signals [33], numerical modeling combined with experimental in situ measurements and observations is still required [36].

In situ injection tests using the mHPP probe (Monitoring Hydromécanique de Pression des Pores) offered the opportunity to investigate the hydromechanical response of a fault zone inside a clay rock mass of low permeability [30]. The experimental observations consist of an original and unique field data set at the decametric scale aiming to bridge the gap between observations at the laboratory and the reservoir scale. We performed hydromechanical simulations using a 3D fully coupled model to study and reproduce one of these tests. While numerical studies dealing with fracture interaction and reactivation already exist in the literature, they make use of the discrete fracture network (DFN) approach at larger scales (reservoir scale) with several assumptions or simplifications (e.g. [18, 60]). Using a representative scale model, we considered realistic fault-related

structures in a deterministic way to interpret and fit real experimental data. To our knowledge, this is one of the first numerical studies dealing with the interpretation of intermediate-scale in situ experiments. Therefore, given the complex structural nature of a fault zone, a numerical modeling study is presented here to estimate the effect of the fractures' connectivity and orientation on the resulting permeability and the mechanical response of the system, including the behavior of the surrounding rock mass. The numerical results were directly compared to field measurements. Based on the modeling observations, another model was set up to perform a sensitivity analysis. In this second model, two intersecting fractures were considered. The main points that we addressed were:

- under which conditions of fracture's orientation and stress and for which hydraulic and mechanical properties, a natural fracture is reactivated?
- what are the dominant activation mechanisms between permeability-controlled and shear-controlled mechanisms?

Combining the two models, useful information was derived to restrain the first-order parameters that control the nature of fractures interaction.

2 In situ experimental setting and injection test results

The in situ field fluid injection experiments were performed at the Tournemire underground research laboratory (URL). The argillaceous formation where the URL nested is 250 m thick and corresponds to sub-horizontal consolidated argillaceous and marly layer of Toarcian and Domerian age [38]. The mineralogical composition of the Tournemire shale consists of 40–50% of phyllosilicates mainly smectite, illite, kaolinite, chlorite and mica, 10–20% of quartz, 10–30% of calcite and 4–8% of feldspars [53]. The shale is characterized by a low porosity, from 8 to 12%, corresponding to a water content of 3.5–5% weight at saturation and a hydraulic conductivity of 10^{-14}–10^{-15} m/s (10^{-21}–10^{-22} m^2) measured on core samples in the laboratory [9].

The injection experiments targeted different parts of a N0-to-170°, 75-to-80°W left-lateral strike-slip fault, 8.5 m thick, intersecting the Toarcian shale formation. The present day in situ stress regime was determined through a series of leak-off tests [13]. The state of stress was estimated as a strike/slip regime with the maximum stress σ_1 being horizontal, oriented N162° ± 15°E and equal to 4 ± 2 MPa. The intermediate stress σ_2 is equal to 3.8 ± 0.4 MPa, and it is the vertical component with a plunge 83–82° and azimuth N072°. The stress σ_3 is the minimum horizontal stress equals to 2.1 ± 1 MPa with a plunge 7–80° and azimuth N072° (Fig. 1a).

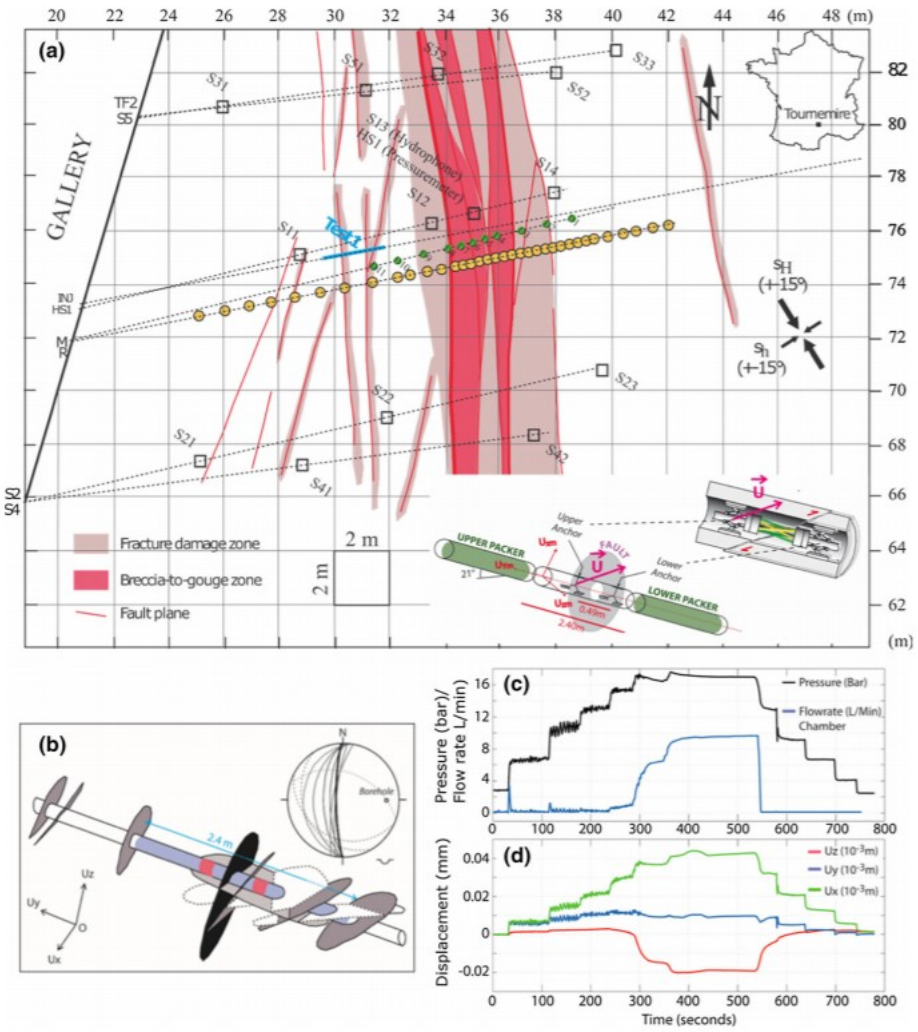

Fig. 1

a Map view of the investigation area: Test 1 interval is shown in blue color along the injection borehole, and the SIMFIP is shown at the right bottom corner. b Test 1 interval geology where the secondary fault is shown in black. c Temporal evolution of the pressure and flow rate (upper graph) and d displacements (lower graph) versus time

The studied test was performed in the west damage zone using the mHPP probe according to the step-rate injection method for fracture in situ properties (SIMFIP) [28]. A 2.4-m injection chamber was isolated by the dual-packer system of the probe (Fig. 1a). The three-dimensional deformation of the targeted fault/fracture intersecting the borehole was captured by an extensometer centered along the axis connecting the two packers (Fig. 1a). According to a step-rate injection protocol, water was injected at a low pressure for a fixed duration. The injection pressure was incremented and held constant, typically for the same duration. After reaching a threshold pressure, called the fracture-opening pressure (FOP), for which a large increase in the flow rate, i.e., higher than 100 mL/min, is observed at constant pressure, a longerduration constant pressure step was performed at

a pressure above this pressure threshold. Then successive step-down experiments followed until the pressure returned to its initial value (Fig. 1c).

The geology of Test 1 interval in the west damage zone is shown in Fig. 1b. It should be noted that even though an important number of fractures were intersected by the test interval, only the ones that were not fully sealed with calcite are shown. An open secondary fault zone oriented N0-to-170, 75-to-80°W characterized by a polished but striated rough surface (black plane in Fig. 1b), was targeted. The fractures that intersected by the borehole interval families displayed three principal orientations N110-to-140, 50°N-to-S, N160, 20-to-40°W and N0-to-20, 40-to-80°W-to-E [30].

The temporal evolution of the fluid pressure, the flow rate and the displacements, recorded by the mechanical probe inside the injection chamber (U_x, U_y, U_z), is presented in Fig. 1c, d (for more details, see [30]). At 237 s and for a pressure equal to 1.5 MPa, a large nonlinear flow rate increase was observed that later reached a quasi-constant value (450–537 s) before the pressure was gradually decreased (Fig. 1c). Before 1.5 MPa, there was no flow rate measured, and at the onset of pressure decrease, the flow rate falls abruptly to zero without any further flow injected in the fault zone for the rest of the injection test. The mechanical response of the test showed that the induced displacements are characterized by a shear component much larger than the normal component (Fig. 1d). The movement inside the fault zone was associated with a left-lateral slip which is in agreement with the measured direction of the principal stresses as measured by [13].

2.1 Coupled hydromechanical analysis of fracture interaction

Taking into account the real position and orientation of the natural fractures in the interval, the effect of fracture interaction is investigated through three model configurations with a total of nine identified “open” fractures (i.e., not fully sealed with calcite) crossing the borehole test interval. We defined three different cases where (a) the first case included all nine fractures intersected by the borehole in the test interval, (b) the second case included the secondary fault (black plane in Fig. 1b) and the sub-vertical family with fractures dipping $> 20°$ and finally (c) in the third case we included the secondary fault along with the sub-horizontal fracture family with fractures dipping $< 20°$. While most of the fractures in the fault zone are dipping toward the west, one fracture was dipping toward the east (N50°–42°E), and it was included in the sub-horizontal fracture family.

2.2 Model setting and simulation protocol

The software used for the numerical calculations is the 3DEC code [32] based on the distinct element method formulation. The fractured rock mass in 3DEC is modeled as an assemblage of discrete blocks which can become deformable by discretizing the domain into finite difference tetrahedral zones. The software uses a dynamic algorithm that solves the equations of motion using the finite difference method. In the study that follows, the

blocks representing the intact material are considered elastic and isotropic with a prescribed stress–strain behavior. The discontinuities in the model are considered as boundary conditions between the blocks. The faults mechanical response follows in our case the generalized Coulomb friction law where the stiffness, the friction angle, the cohesive, the tensile strength and the dilation angle need to be defined. In the elastic range, the normal and shear stiffness of the fault determine the fault's response according to the following equations:

$$\Delta F^{\mathrm{n}} = -K_{\mathrm{n}} \Delta U^{\mathrm{n}} A_{\mathrm{c}} \tag{1}$$

$$\Delta F^{\mathrm{s}} = -K_{\mathrm{s}} \Delta U^{\mathrm{s}} A_{\mathrm{c}} \tag{2}$$

where K_{n} and K_{s} (Pa/m) are the fault normal and shear stiffness, respectively, A_{c} is the contact area, ΔU^{n} and ΔU^{s} are the normal and shear displacement increments and ΔF^{n} and ΔF^{s} are the normal and shear force increments. In the plastic range, a maximum shear force is defined as:

$$F^{\mathrm{s}}_{\max} = cA_{\mathrm{c}} + F^{\mathrm{n}} \tan\varphi \tag{3}$$

where c is the fault cohesion and φ the friction angle. The normal tensile force is limited to:

$$T_{\max} = -TA_{\mathrm{c}} \tag{4}$$

where T is the fault tensile strength. As soon as the sub-contact fails, either in shear or tensile mode, the tensile strength and the cohesion are set to zero simulating a "displacement weakening" joint. At the onset of shear failure, the dilation angle is mobilized according to:

$$\Delta U^{\mathrm{n}}\,(\mathrm{dil}) = \Delta \tan\psi \tag{5}$$

where ψ is the dilation angle.

For hydromechanical analysis and fluid flow calculations, the discontinuity geometrically corresponds to a two-dimensional flow plane. Fluid flow is only occurring along the discontinuity plane meaning that the intact surrounding material is impermeable. The flow rate per unit width of the discontinuity is computed through the "modified" cubic law [59]:

$$q = -\frac{u_{\mathrm{h}}^3 \rho g}{12\mu} \nabla_{\mathrm{h}} = -k_{\mathrm{h}} \nabla_{\mathrm{h}} \tag{6}$$

where u_{h} is the equivalent hydraulic aperture of the idealized fracture (m), k_{h} is the hydraulic conductivity of the fracture (m/s), ∇_{h} is the hydraulic gradient, ρ is the fluid density (kg/m^3), g is the gravitational acceleration (m/s^2) and μ is the fluid dynamic viscosity (Pa s). Regarding the calculation

of the hydraulic aperture throughout the simulation, in the elastic range, its value is updated as a function of the effective normal stress:

$$u_{\mathrm{he}} = u_{\mathrm{h0}} + f\frac{\Delta\sigma'_{\mathrm{n}}}{K_{\mathrm{n}}} \tag{7}$$

where u_{h0} is the initial hydraulic aperture, $\Delta\sigma'_n$ is the effective normal stress variation and f is a factor reflecting the influence of the roughness. The factor f is taken as 1 in 3DEC meaning that the fracture walls are planar. In the plastic range, the effect of dilation is also accounted for as the fault slips:

$$u_{\mathrm{hp}} = u_{\mathrm{h0}} + f\frac{\Delta\sigma'_{\mathrm{n}}}{K_{\mathrm{n}}} + f u_{\mathrm{hs}} \tag{8}$$

where u_{hs} is the dilation-induced normal displacement. For our calculations, we considered that the fluid is only propagating along the parts of the discontinuities' planes that have failed in tensile or shear mode. This means that initially the fractures of the model are considered to be closed and therefore not saturated. Such an assumption can be justified by the initial low permeability of the secondary fault (black plane in Fig. 1b) measured in situ being equal to 10^{-17} m^2 (Y. Guglielmi, personal communication). A complete coupled solution is adopted in our calculations based on a simultaneous fluid flow/mechanical calculation. More specifically, the hydromechanical model in 3DEC is quasi-static meaning that the mechanical model is in equilibrium for the current distribution the pore pressures. Therefore, for each flow timestep, there is a number of mechanical timesteps executed in order to reach mechanical equilibrium. Once the updated geometries have been determined from the mechanical calculations, the new values can be defined for the apertures of the discontinuities. After the flow rates have been calculated according to Eq. (6), the pressure on each gridpoint along the discontinuity is updated.

A numerical model has been set up using as a reference case the model including all the fractures intersected by the borehole in the injection interval (Fig. 2a). Figure 2b shows the second case where the secondary fault is modeled along with the sub-vertical fracture family, and Fig. 2c shows the last case with the secondary fault and the sub-horizontal family. The model corresponds to a cube of 10 m edge length. The size of the model was determined in [30] as the best-fit solution in terms of hydraulic boundaries, better matching the measurements. The six faces of the 3D domain are submitted to the in situ stress field described in Sect. 2 according to previous measurements [13], and an initial pore pressure value of 0.2 MPa was applied to the model domain, close to the observed in situ fluid pressure conditions [20]. For the sake of simplicity, the borehole and the injection chamber are not explicitly represented. The pressurization of the intersected fractures is achieved by placing injection points where

the pressure is controlled at each intersection point between borehole and fractures, and the resulting flow rate is equal to the sum of the flow rates recorded for each fracture–borehole intersection points. For the modeling of the interval fractures in the same model, the two following assumptions were made: i) The fractures in the model are persistent (> 10 m). Their real size is not accounted for, and consequently, a high connectivity is assumed since the considered fractures are probably much smaller than the secondary fault plane; ii) all the fractures inside the model are characterized by the same material properties. The injection was simulated by imposing a step-rate fluid pressure loading at the center of the model (gridpoint 0, 0, 0) corresponding to the loading protocol (see Fig. 1c) applied during the field experiment. The properties of the rock matrix and fractures were calibrated based on the experimental recordings during an injection test inside an identified and characterized fault zone [30]. These values represent the best-fit set of parameters and are summarized in Table 1.

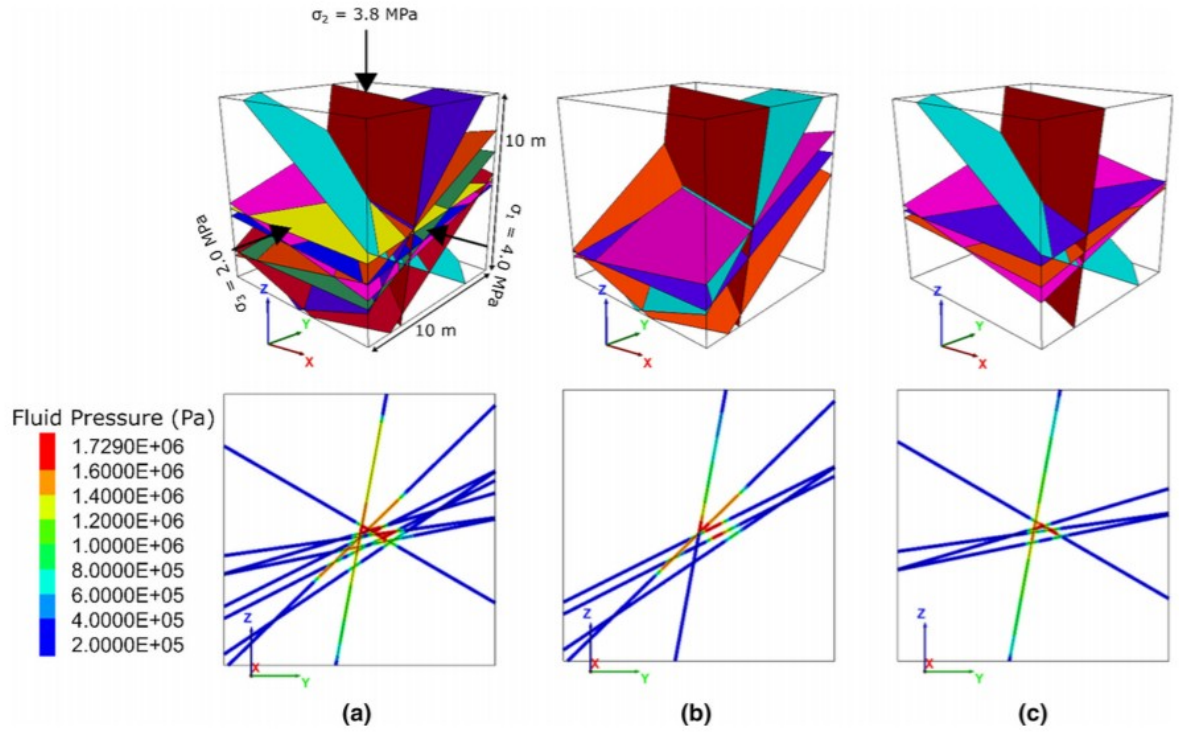

Fig. 2 Model geometry (top) and fluid pressure distribution shown along a vertical plane at the center of the model (bottom) for $t = 537$ s corresponding to the end of the highest pressure test, for **a** the secondary fault plane with the sub-vertical and sub-horizontal families, **b** secondary fault plane with the sub-vertical family, **c** secondary fault plane with the sub-horizontal family

Table 1 Parameters' values of the numerical model [28]

Rock matrix properties		
Density	ρ	2500 kg/m^3
Bulk modulus	K	5.15×10^6 Pa
Shear modulus	G	3.94×10^6 Pa
Fault plane properties		
Normal stiffness	K_n	200×10^9 Pa/m
Shear stiffness	K_s	4×10^9 Pa/m
Friction angle	φ	35°
Cohesion	c	0
Dilation angle	ψ	5°
Initial hydraulic aperture	u_{h0}	3×10^{-5} m
Fluid properties		
Bulk modulus	K_f	2×10^9 Pa
Density	ρ_f	1000 kg/m^3
Dynamic viscosity	μ	10^{-3} Pa × s

The properties of the rock matrix and fractures were calibrated based on the experimental recording done during an injection test inside an identified and characterized fault zone [30]. These values represent the best-fit set of parameters and are summarized in Table 1. Normal and shear stiffness of the discontinuities were initially estimated using the measured displacement versus pressure relationships in the elastic range. The static friction value assigned was calculated assuming a cohesionless fault surface according to the Coulomb criterion and for the in situ stress field [13]. The fault's dilation angle was derived by the magnitude of the measured normal and shear displacements during slip. Regarding the initial hydraulic aperture value, this was estimated by the transmissivity value recovered at the first part of the test (below the fracture-opening pressure, FOP) and according to the cubic law (Eq. 6 and [59]). Nevertheless, as the normal deformation during slip was small compared to the increase in the observed flow rate, the hydraulic aperture increase could not be solely attributed to the dilation during slip. Therefore, in the model, a simple relationship was considered for the hydraulic aperture in the plastic range:

$$u_{\mathrm{hs}} = B \times u_{\mathrm{he}} \tag{9}$$

where B was evaluated as a function of measured flow rate and pressure and was set to be equal to 7 to a better match between the calculated and the measured values. The elastic properties of the intact material were found to slightly influence the behavior of the fault at failure probably due to the simple Coulomb relationships conditioning slip and flow rate variations. For more details on the calibration of the model and the material constants, the reader is referred to [30].

3 Results

As mentioned before, besides the model containing the totality of the fractures identified crossing the injection chamber (Fig. 2a, case a), the contribution of each fracture family's orientation is also tested. More specifically, the secondary fault plane (i.e., the brown plane Fig. 2a, cases a, b and c) is modeled together with the sub-vertical fracture family only in a second configuration (Fig. 2b, case b), and in a third configuration, the fault is modeled with the sub-horizontal fracture family only (Fig. 2c, case c).

In all cases, the fracture plane that was mostly affected by the fluid pressurization is the secondary fault, i.e., the brown plane (Fig. 2, bottom). The rest of the fractures appear to be locally pressurized only at the injection point (point of intersection with the borehole) or at the intersection points with the pressurized fault but without any propagation taking place within their planes. So far, as the properties of the fractures considered are identical, the effect of the orientation with respect to the stress field is the controlling parameter. Keeping in mind that $\sigma_{min} = \sigma_y$ which is almost normal to the secondary fault, the fractures characterized by a dip angle lower than 40° are not activated even for identical hydromechanical properties and with more favorable orientation for shear reactivation in the *z*–*y* plane shown.

The temporal evolution of the displacements calculated for these three configurations within the fluid injection zone is then compared to the experimental data (Fig. 3). While the displacement in the *x*-direction (green lines) is quite well represented for the two first cases (Fig. 3a, b left), it is underestimated in the last case (Fig. 3c left), i.e., when ignoring the sub-horizontal fracture set. Regarding the horizontal displacements (*y*-direction, purple curves) and the vertical displacements (*z*-direction, orange curves), the best results are obtained when the fault plane is in association with the sub-vertical fracture set (Fig. 3b left).

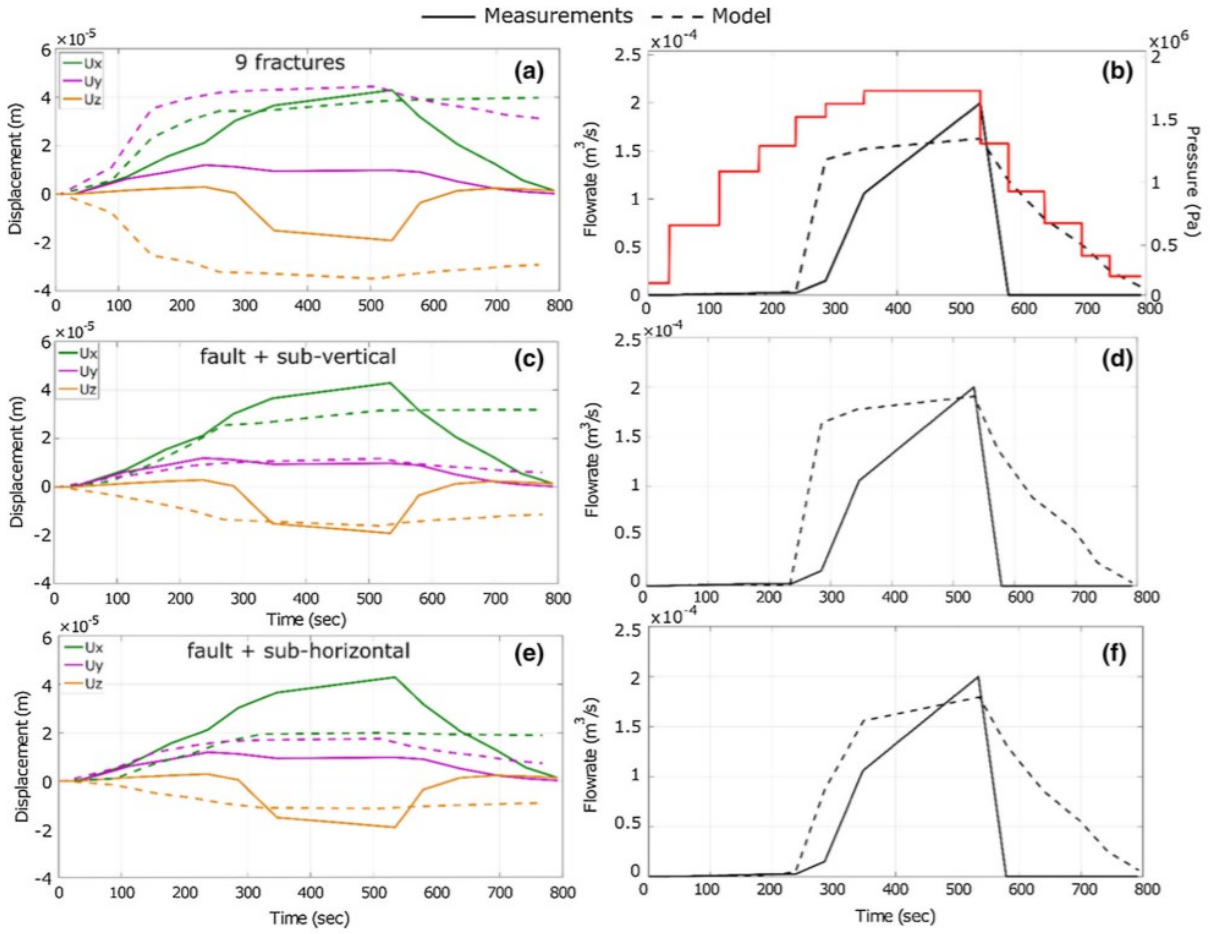

Fig. 3

Displacements and flow rate versus time for: Top a and b: secondary fault plane with the sub-vertical and sub-horizontal families (9 fractures in total), middle c and d: secondary fault plane with the sub-vertical family only, bottom e and f: secondary fault plane w with the sub-horizontal family only. On the left a, c and e, the temporal evolution of the displacements for the three components are plotted, and on the right b, d and f the temporal evolution of the flow rate and the applied fluid pressure in red (presented in b). Dashed lines correspond to the numerical model results and the solid lines for the experimental data sets

In terms of flow rate response, reminding that the injection fluid pressure is imposed, an abrupt increase is observed for all cases (Fig. 3 right) for time $t = 200$ s. This one is higher than the one observed in the experimental data set, because in all cases the horizontal displacement, i.e., the y-direction (orange lines) which corresponds to the aperture of the fracture set in the minimum stress direction, increases earlier in the model. This strong nonlinearity response observed in the experiments is not well reproduced by the model. Finally, the constant flow rate value obtained in the models is closed to the one observed experimentally, until the unloading takes place (i.e., end of the fluid injection sequence).

3.1 Fracture interaction generic model—sensitivity study

From the complex multi-fracture model, it could be seen that the orientation of the fracture sets depending on the principal stress directions plays a major role in their hydromechanical response. However, the complexity of the models described at the previous section makes it difficult to be used for a sensitivity analyses. In order to quantify the coupled effects between the in situ conditions and the fracture properties, a simpler model is now set up to investigate in details the interaction mechanisms between a natural fracture intersected by a fluid-driven fracture orientated perpendicular to the minimum stress. In natural conditions, this fluid-driven fracture could be created by the overpressurized geo-stored fluids or by an extensional vein fracture in a fault environment formed during preseismic stages [15, 24, 25, 49, 50, 51]. In the numerical simulations, the cohesion and the tensile strength of the fluid-driven fracture are higher than the intersected natural fracture's ones.

3.2 Model description

The model corresponds to a parallelepiped of 20 m × 10 m × 10 m cut by two intersecting fractures, respectively, mentioned as hydraulic fracture (black plane in Fig. 4) and as the natural fracture (gray plane in Fig. 4). The hydraulic fracture is favorably oriented, i.e., in the direction of the maximum stress and perpendicular to the minimum stress, facilitating the propagation of fluid.

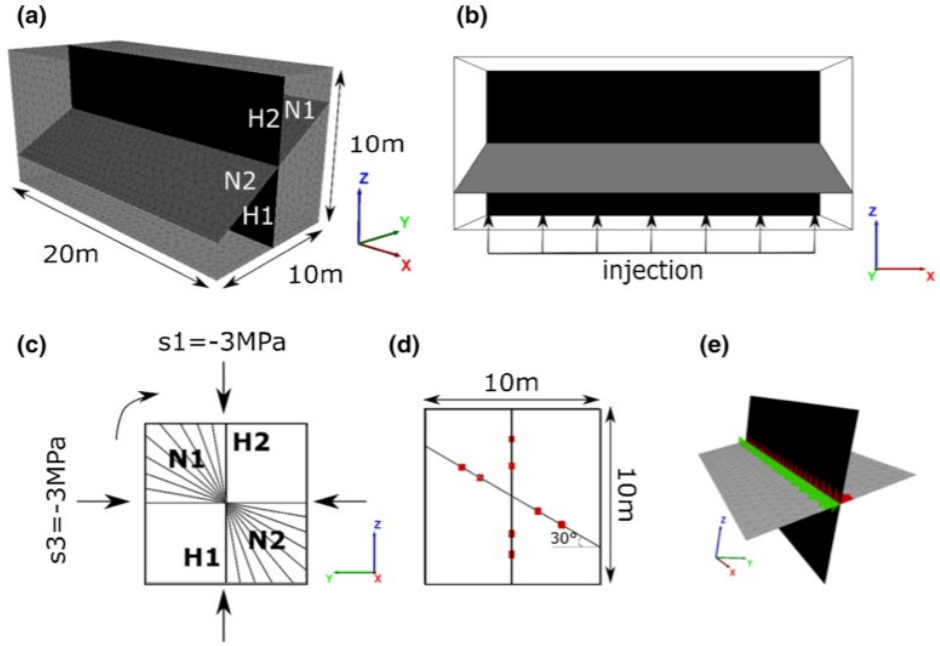

Fig. 4 **a** Geometry of the numerical model, **b** application of injection pressure at the bottom of the hydraulic fracture plane, **c** stress field and rotation of the natural fracture dip from 0° (perpendicular to the hydraulic fracture) to 80° (almost parallel to the hydraulic fracture), **d** fluid pressure and displacement recording points (red squares) along the hydraulic and natural fractures, **e** flow zones (red and green) around the intersection for the calculation of the flow rate for each half-plane

The effect of the orientation of the natural fracture is investigated by rotating the natural fracture plane's dip. The dip angle rotation is measured from the horizontal, and it is varied from 0° to 80° with increments of 10° (Fig. 4c). For a dip angle of 0°, the natural fracture is horizontal, thus perpendicular to the hydraulic fracture and the vertical stress (σ_1). For a dip angle of 80° the fracture is almost vertical, thus parallel to the hydraulic fracture. The analysis is performed with a model aligned with principal stress directions, meaning that only fracture planes having poles within the σ_1–σ_3 plane are considered [16]. An initial pore pressure is applied inside the model, and a vertical pore pressure gradient is applied from the bottom to the top model boundary to initiate the fluid propagation. The other boundaries are impermeable. The injection time is 15 s long, which corresponds to the time, needed to reach a steady-state flow regime.

To obtain a detailed analysis, the two planes of the model are both divided into half-planes (Fig. 4a):

- The hydraulic fracture is divided into half-plane H1 before the intersection and half-plane H2 above the intersection with the natural fracture.
- Similarly, the natural fracture is divided into half-plane N1 on the left of the intersection and into half-plane N2 on the right of the intersection with the vertical hydraulic fracture.

Throughout the calculation and in order to capture the mechanical response of the natural fracture, the normal and shear displacement and the flow rate magnitudes are recorded for each half-plane (Fig. 4d, e). For the hydraulic fracture, the flow rate is computed as a surface average for a group of zones along H1 half-plane just below the intersection with the natural fracture and for a group of zones along H2 half-plane just above the intersection with the natural fracture. For the natural fracture, the flow rate is calculated just after the intersection with the hydraulic fracture on both sides. This will provide the quantitative amount of fluid crossing or not the natural fracture.

3.3 Reference case

As a reference case, the stress field is considered isotropic with $\sigma_x = \sigma_y = \sigma_z = -3$ MPa and the dip angle of the natural fracture is 30°. The intact rock properties correspond to transversely isotropic shale material properties induced by the bedding planes in shales ([10] and Table 2). The bedding plane-induced anisotropy is considered horizontal with the directions 1 and 3 being the directions parallel and normal to the bedding, respectively. The properties of the natural fracture are in the range of values considered in the previous model. It should be noted at this point that the hydraulic aperture is not increasing in the calculations by a factor B as assumed in the previous model (Eq. 9).

Table 2 Boundary conditions and material properties for the reference case (dip angle = 30°)

Size of the block ($L \times l \times H$)			
20 m × 10 m × 10 m			
Boundary conditions			
Stress field			
$\sigma_x = -3 \times 10^6$ Pa, $\sigma_y = -3 \times 10^6$ Pa, $\sigma_z = -3 \times 10^6$ Pa			
Initial pore pressure: pp = 1.2×10^6 Pa			
Injection pore pressure: $pp_{inj} = 4.5 \times 10^6$ Pa			
Rock matrix properties			
Density		P	2500 kg/m^3
Young's modulus parallel to bedding		$E_1 = E_2$	7.2×10^9 Pa
Young's modulus normal to bedding		E_3	2.8×10^9 Pa
Poisson's ratio parallel to bedding		ν_{12}	0.24
Poisson's ratio normal to bedding		$\nu_{13} = \nu_{23}$	0.33
Shear modulus parallel to the bedding		G_{12}	2.9×10^9 Pa
Shear modulus normal to the bedding		$G_{13} = G_{23}$	1.2×10^9 Pa
		Fracture properties	
		"Hydraulic" fracture	"Natural" fracture
Normal stiffness	K_n	200×10^9 Pa/m	200×10^9 Pa/m
Shear stiffness	K_s	4×10^9 Pa/m	4×10^9 Pa/m
Friction angle	Φ	20°	20°
Cohesion	C	3×10^6 Pa	0
Tensile strength	σ_t	10^6 Pa	0
Initial hydraulic aperture	u_{h0}	1×10^{-4} m	1×10^{-4} m
Fluid properties			
Bulk modulus		K_f	2×10^9 Pa
Density		ρ_f	1000 kg/m^3
Dynamic viscosity		M	10^{-3} Pa × s

The calculated time variations of fluid pressure, normal and shear displacements and flow rate in the four half-planes H1, H2, N1 and N2 are shown in Fig. 5.

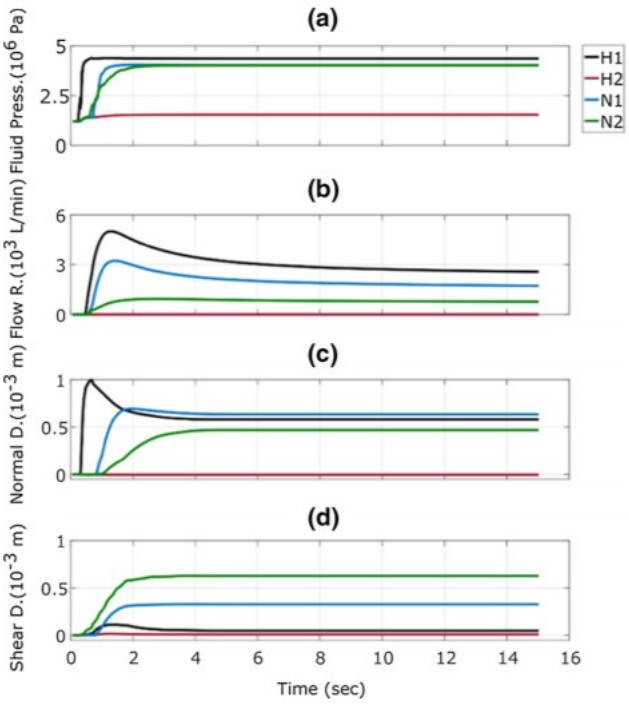

Fig. 5 From top to bottom: **a** fracture fluid pressure, **b** flow rate, **c** normal displacement, **d** shear displacement versus time for the half-planes H1, H2, N1, N2

The fluid pressures inside H1, N1 and N2 have reached approximately the injection pressure of 4.5 MPa imposed at the bottom of the fluid-driven fracture (see also Fig. 6). No pressure variation occurred in H2 showing that the hydraulic fracture did not propagate above the intersection with the natural fracture. The flow rate in H1 and N1 shows a peak which is explained by the high hydraulic gradient as the fluid preferentially propagates from H1 to N1. After 15 s of injection, all recorded signals have reached a steady-state value; the fluid has propagated inside the fractures following a preferential flow path to connect with the model boundaries.

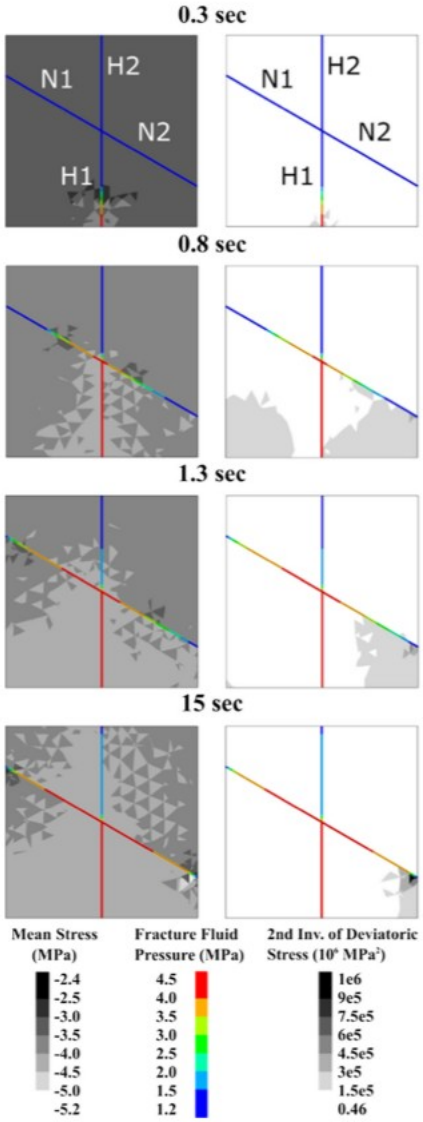

Fig. 6

Evolution of the mean stress (left column), the second invariant of differential stress (right column) and of the fracture fluid pressure at different injection times

Considering the mean stress and the second invariant of the differential stress, these are defined according to Eqs. (10, 11):

$$\sigma_{\mathrm{m}} = \frac{1}{3}(\sigma_{11} + \sigma_{22} + \sigma_{33}) \tag{10}$$

$$J_2 = \frac{1}{6}\left[(\sigma_{11} - \sigma_{22})^2 + (\sigma_{22} - \sigma_{33})^2 + (\sigma_{11} - \sigma_{33})^2\right] + \sigma_{12}^2 \tag{11}$$

where σ_{11}, σ_{22}, σ_{33} are the maximum, intermediate and minimum principal stress components, respectively, and σ_{12} is the stress acting in the direction 2 on the surface that is oriented perpendicular to direction 1. The evolution of the mean stress and the second invariant of the differential stress inside

the model are shown at different time steps in Fig. 6. Fluid pressure in the fractures is superimposed to the stress contour maps. The negative mean stress values correspond to compressive stresses.

A hydraulic fracture when interacting with a natural fracture can either cross it or stop due to the mechanical or hydraulic or hydromechanical reactivation of the natural fracture. For 30° of dip orientation and for a homogeneous stress field, the hydraulic fracture does not cross the natural fracture. Accordingly, the calculated flow rate signals show that the flow rate of the half-plane H2 (red line in Fig. 5b) is null by the end of the calculation, while the flow rate of the natural fracture's segments is increasing during the injection (blue and green lines in Fig. 5b). Hence the natural fracture is hydraulically activated and the propagation of the hydraulic fracture becomes impossible farther from the intersection. Both the normal and shear deformation of N1 and N2 half-planes show opposite behaviors and significantly different values. There is a higher normal opening of N1 compared to N2, with final apertures 6 and 4 times higher than initial, respectively, in N1 and N2. Shear amplitude of N1 and N2 is opposite to normal amplitude variations. N2 displays the smaller normal opening and the higher shear displacement. One can observe that shear displacement is also taking place in the H1 half-plane at earlier time steps of the injection even though the hydraulic fracture is supposed to grow under zero shear. Reminding at this point that the hydraulic fracture is growing along an imposed predefined plane and that the surrounding medium is not homogeneous, we would expect some stress alterations as the pressure increases and the hydraulic fracture deforms. If the hydraulic fracture plane was allowed to deviate to a more favorable orientation imposed by the intact matrix anisotropy, it is possible that there would not be any shear displacement recorded along the plane.

In Fig. 6, the evolution of the mean stress and of the second invariant of the differential stress is illustrated for four different times during the simulation. As the fluid propagates and the hydraulic fracture plane dilates, the surrounding stress field is affected and the mean stress magnitude increases (Fig. 6 on the left). This is a result of the increase in the fluid pressure inside the hydraulic fracture plane and the plane's subsequent deformation. As the plane deforms, the total minimum stress inside the rock matrix will become higher. Due to the Poisson's ratio, an increase in the maximum and intermediate stresses is also observed leading to an increase in the mean stress value. As the fluid front approaches the intersection with the natural one (0.8 s in Fig. 6), the increase in the mean stress magnitude is affecting a larger area of N2 compared to N1. This explains the delay in the fluid propagation inside N2, characterized by the delay in the fluid pressure variation and by the lower flow rate variation (Fig. 5a, b). At $t = 0.8$ s and $t = 1.3$ s, there is an increase in the second invariant of the differential stress close to the bottom corners of the model (Fig. 6 on the right) affecting a surface area of N2 away from the intersection. This differential stress

increase originates from the hydraulic fracture propagation and the induced total stress changes that will also affect the deformation of the intact surrounding material. Close to the bottom corners of the model, the intact material is deforming in shear contributing to the increase in the differential component of the stress tensor. As a result, at 0.3, 0.8 and 1.3 s, N2 appears to deform in shear well before conducting the fluid.

3.4 Effect of natural fracture's orientation

Figure 7a shows that flow rate in H2 never increases highlighting that the hydraulic fracture never crosses the natural fracture for all possible orientations of the natural fracture. The growth of the hydraulic fracture is stopped at the intersection with the natural fracture. The half-plane H2 is only exhibiting some negligible shear displacement (red line in Fig. 7c) as a result of stress transfer mechanisms.

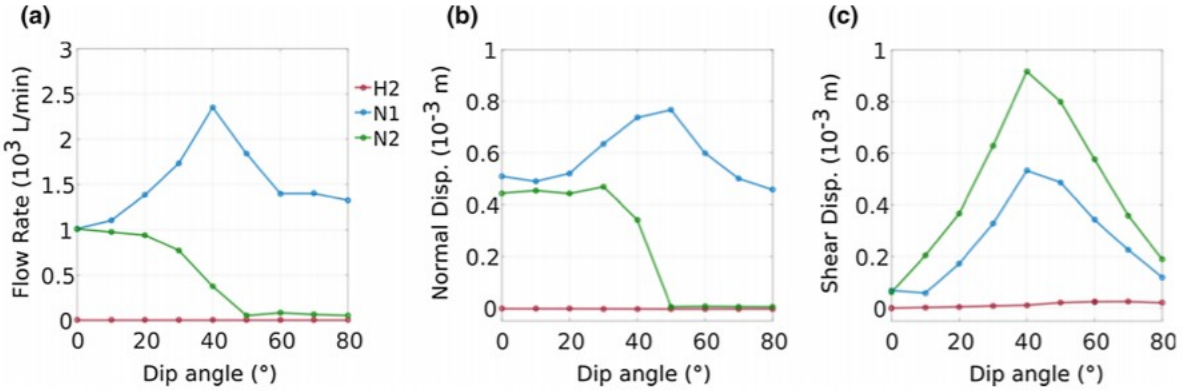

Fig. 7 From left to right; **a** variation of the flow rate, **b** the normal displacement and **c** the shear displacement versus the dip angle of the natural fracture at the end of the simulation for half-planes H1, H2, N1, N2

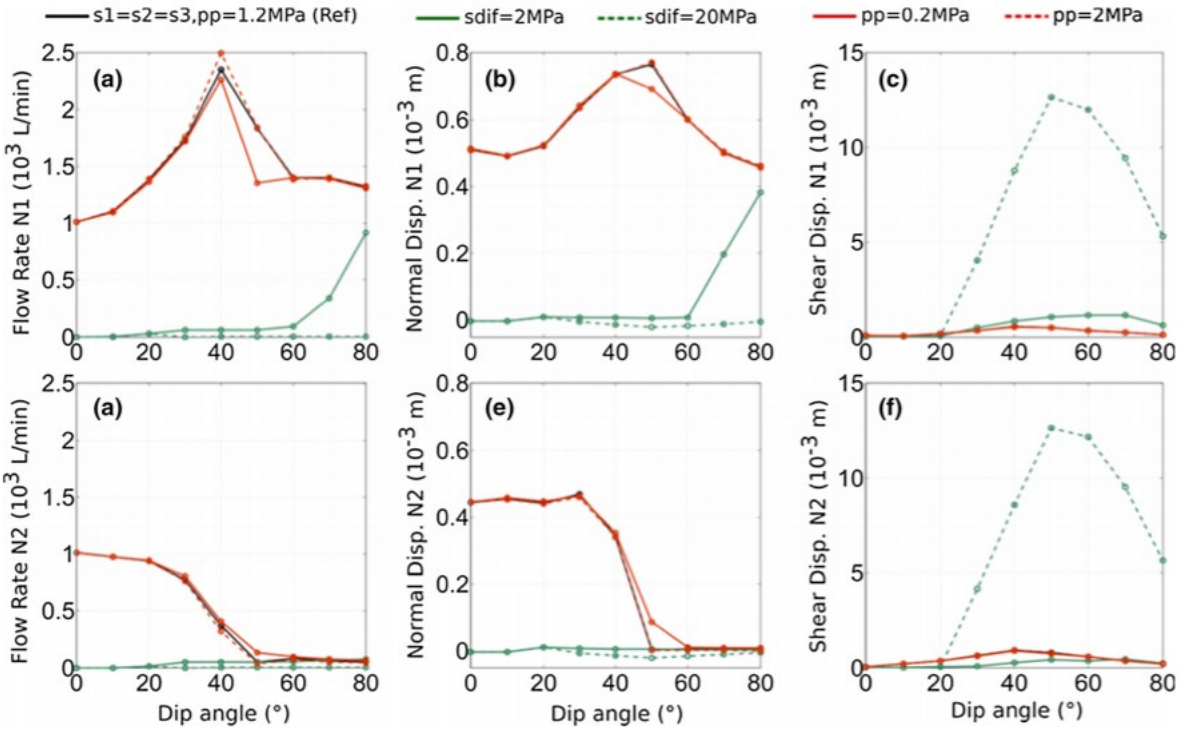

Fig. 8 Variation of flow rate (left column), normal displacement (middle column) and shear displacement (right column) for N1 (top line) and N2 (bottom line) as a function of stress and initial fluid pore pressure inside the fractures

As N1 dilates, an increase and reorientation of the total stresses take place in the block between N1 and H2. Due to the isotropic stress state acting on the fracture system, we can observe a symmetrical response in terms of flow rate, normal and shear displacement magnitudes of the half-plane N1 above and below a critical rotation angle approximately of 40°. N1 stays hydraulically active for all the natural fractures dip angles with a maximum value at the 40° dip angle, where the maximum shear displacement is also recorded for the same half-plane. The shear displacement of the half-plane N1 is increasing around 20°, which is coherent with the friction value of 20° assigned to the fracture. On the other hand, the behavior of the half-plane N2 is dominated by the normal opening of the hydraulic fracture and the consequent stress transfer. For higher dip angles and as the plane gets sub-parallel to the hydraulic fracture plane, N2 hydraulic activation becomes highly limited under the action of an increased normal stress. For all possible natural fracture orientations, N2 shear displacement (green line in Fig. 7c) is higher than N1 (blue line in Fig. 7c). As explained in the reference case, stress transfer effects determine the response of N2 by promoting shear displacement along the part of the half-plane that is closer to the model boundaries (Fig. 6, right column).

3.5 Effect of the initial loading and stress conditions

In order to estimate the effect of the stress field, the maximum stress (σ_1) and the pore pressure are varied considering four cases:

- A differential stress of 2 MPa (corresponding to an increase of σ_1 from 3 to 5 MPa)
- A differential stress of 20 MPa (corresponding to an increase of σ_1 from 3 to 23 MPa)
- An initial fracture pore pressure of 0.2 MPa
- An initial fracture pore pressure of 2 MPa

For an increase in 2 MPa of the differential stress, the flow rate is highly limited for $\leq 60°$ N1 and N2 dip angles (green line in Fig. 8a, d). Above 60°, the hydraulic fracture growth is prohibiting the hydraulic activation of N2 (green line in Fig. 8d) due to total stress increase induced. Below 60°, N1 and N2 offer the same hydromechanical responses.

For a principal stress difference of 20 MPa, the natural fracture remains hydraulically inactive for all the dip angles orientation (green dashed lines in Fig. 8a, d). The two segments of the natural fracture respond in the same mechanical way. It appears that for orientation angles of 30°–70°, the natural fracture is undergoing a mechanical closure (negative values for the green dashed curves in Fig. 8b, e) accompanied by a large slip (green dashed lines in Fig. 8c, f). For the same range of dip angles, the fracture reactivation is not reaching the intersection with the natural fracture. This is shown in Fig. 9 where the stress tensor components magnitudes inside the model can be seen together with the fluid pressure along the fracture for 20° (Fig. 9 left) and 50° dip angle (Fig. 9 right), for the area around the intersection. Under such a high differential stress and for critical fracture orientations (in this case $> 20°$), the natural fracture is slipping well before the injection and propagation takes place. The stress field in the intact rock is reorganized with the minimum stress magnitude increasing significantly. Hence, a higher pressure is needed for the propagation of the hydraulic fracture.

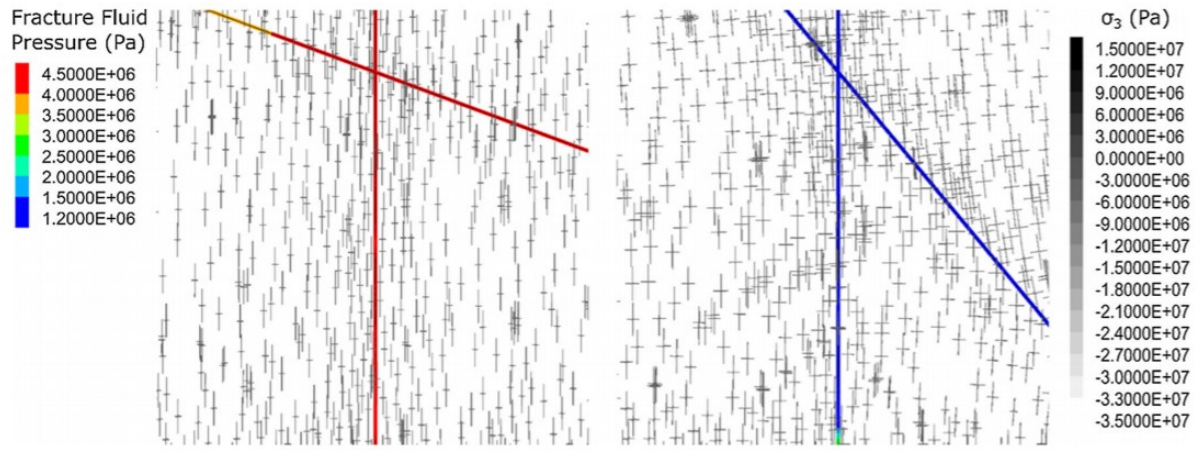

Fig. 9 Stress tensor magnitudes inside the model and fluid pressure variation along the fracture for 20° (left) and 50° (right) natural fracture dip angle

Varying the initial pore pressure of the formation shows that no significant impact of the initial fluid pore pressure value is observed (red and red

dashed curves in Fig. 8), while there is a strong effect of the stress. In cases of extreme stress difference, the reactivation of the fracture can be stopped due to the slip of the natural fracture and the subsequent increase in the minimum stress. For a non-hydrostatic stress field, the far-field stresses will determine the response of the system. For slightly higher differential stresses, the stress transfer effects will be of second-order importance inside the model, and it is only for very low angles between the natural fracture and the hydraulic fracture that the total stress changes will limit the natural fracture's reactivation ($< 30°$). In the case of high differential stresses, the natural fracture will be at failure for a wide range of critical orientations even before the propagation of the hydraulic fracture. Stress magnitude alterations that are promoted can affect significantly the propagation of the hydraulic fracture.

3.6 Effect of the material properties

3.6.1 Mechanical properties of the natural discontinuity

The elastic normal and shear stiffness of the natural fracture do not influence much the response of the fracture (Fig. 10). For a 10 times lower shear stiffness, N1 appears more permeable (red curve in Fig. 10a) and N2 less permeable for a dip angle of 40°–60° (red curve in Fig. 10d). The normal deformation of the half-planes follows more or less the flow rate evolution. Shear displacement in N1 is unchanged, whereas shear displacement in N2 changes according to the assigned shear stiffness value. It points out the difference between the induced shear displacements of each half-plane. More specifically, N1 shear displacement is the result of effective stress variation not dependent on the elastic properties of the natural fracture. On the other hand, above a critical angle, shear displacement of N2 induced by the fluid-driven fracture propagation is determined by the elastic properties of the fracture. As the fluid is not propagating along N2 above 40°, the half-plane is still in the elastic range, under the influence of elastic stress changes. Thus, depending on the value of the shear stiffness, the shear displacement is going to be higher or lower than the reference case (red lines in Fig. 10f).

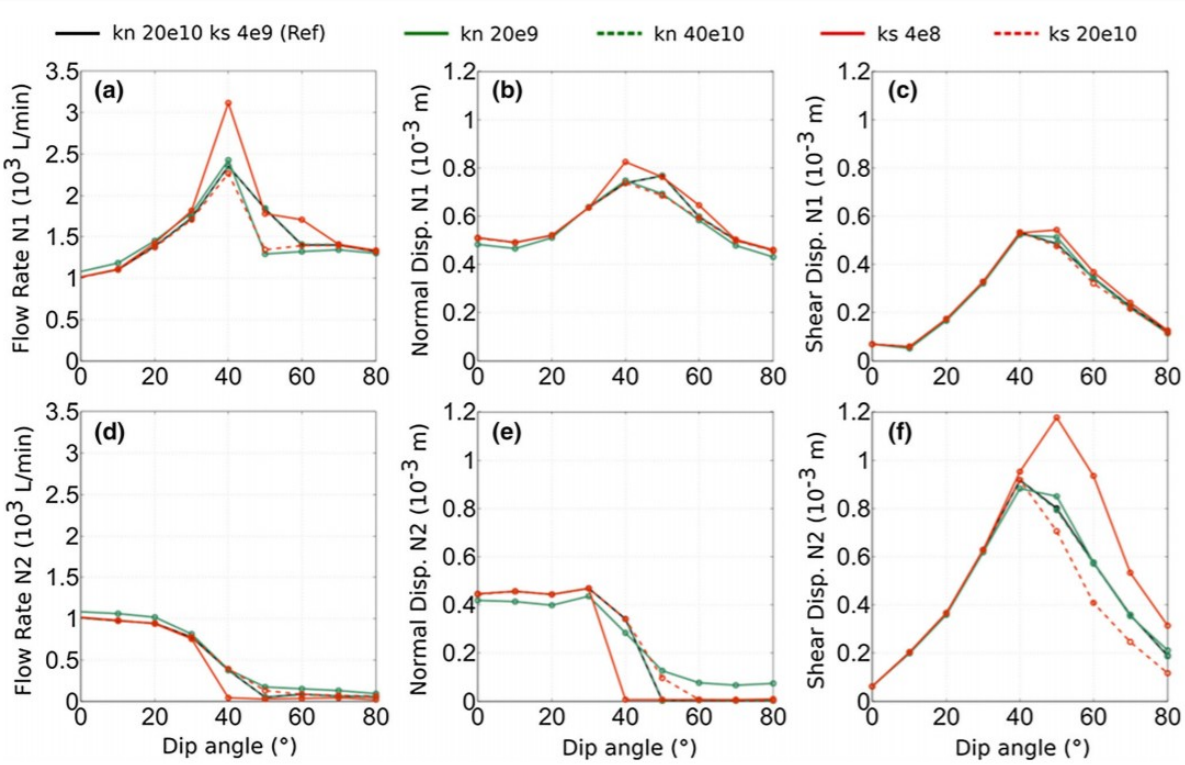

Fig. 10 Variation of flow rate (left column), normal displacement (middle column) and shear displacement (right column) for N1 (top line) and N2 (bottom line) as a function of the elastic properties of the natural fracture

The effect of friction variations on the shear displacement of N1 and N2 is almost identical to the reference case except for a very low friction angle ≤ 10° (red curves in Fig. 11). Below a friction angle of 10°, the half-planes are influenced in a different way. At 40° of orientation, N1 is more conductive than the reference case whereas N2 is not activated. The effect of the variation of the dilation angle on N1 hydromechanical response is negligible as by the end of the calculation, the normal opening of the fracture will have reached its maximum possible value for all cases considered (Fig. 11b, c). The normal deformation of N2 is increased for higher dilation angles and higher dip angles (green dashed line in Fig. 11e), accompanied by a slightly enhanced resulting permeability (green dashed line in Fig. 11d).

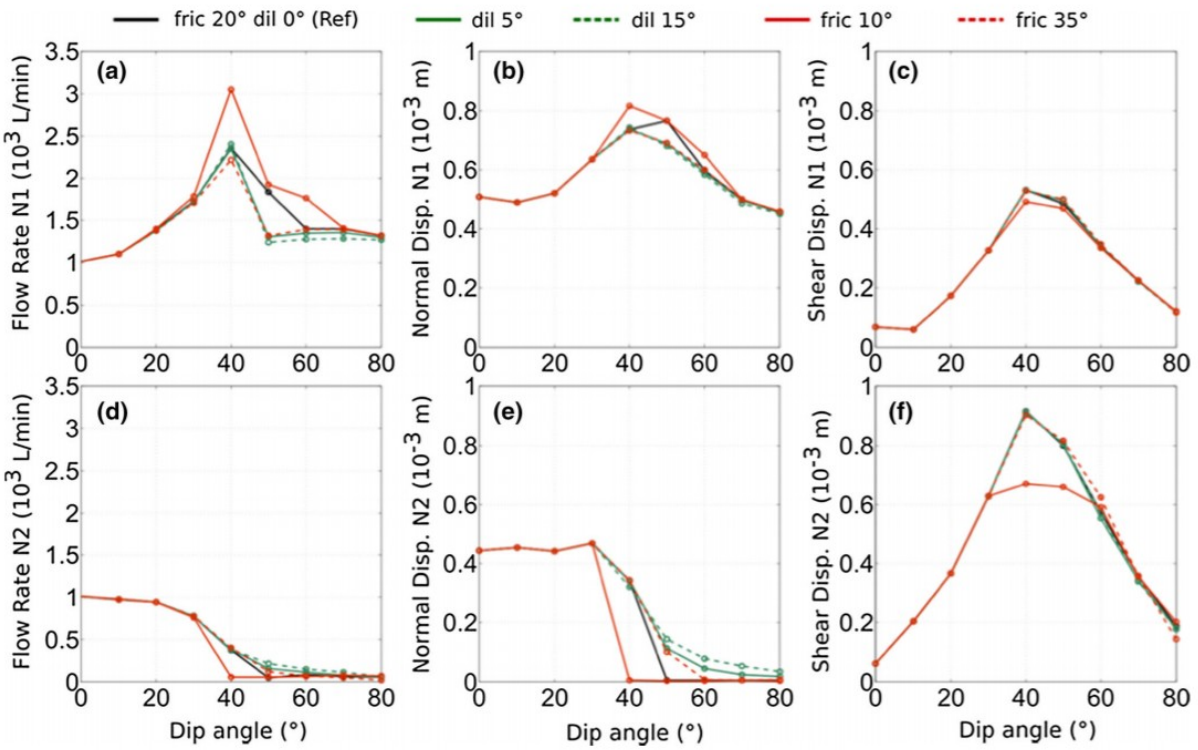

Fig. 11 Variation of flow rate (left column), normal displacement (middle column) and shear displacement (right column) for N1 (top line) and N2 (bottom line) as a function of the strength properties of the natural fracture

3.7 Elastic properties of the intact material

In the reference case, the surrounding intact material of the model is considered as transversely isotropic, accounting for the anisotropy induced by the bedding planes. Two cases of isotropic material are examined with a Young's modulus $E = E_1$ and a Poisson's ratio $v = v_{12}$ (green curves in Fig. 12) and $E = E_3$ and $v = v_{13} = v_{23}$ (blue curves in Fig. 12). In addition, a bimaterial model is considered as a third configuration where the natural fracture is a bimaterial interface separating two media with different elastic properties (red curves in Fig. 12). Above the natural fracture, the medium is characterized by $E = E_3$ and $v = v_{13} = v_{23}$ and below the fracture, the second medium is characterized by $E = E_1$ and $v = v_{12}$. When the intact material is isotropic and stiffer ($E = E_1$), the normal deformation and flow rate magnitudes are increased for both half-planes (green curves in Fig. 12a, b, d, e). On the other hand, the shear deformation appears limited (green lines in Fig. 12c, f). In the isotropic and softer intact material case, the calculated flow rate and normal displacement are higher than the reference case (blue lines in Fig. 12a, b, d, e). N1 shear deformation stays generally lower than the reference case in this configuration (blue line in Fig. 12c) whereas N2 shear deformation increases (blue curve in Fig. 12f). Similar trends are observed for the bimaterial model (red lines in Fig. 12). It is shown that the flow rate calculated in the half-planes N1 and N2 is higher when the planes are surrounded by the isotropic material or when a bimaterial interface is

considered (Fig. 12a, d). The material is more compliant in the isotropic and the bimaterial cases resulting in higher calculated magnitudes of flow rate and normal deformation of the half-plane N1. Considering the response of N2, it is again conditioned by the stress transfer due to the deformation of the hydraulic fracture. Nevertheless, depending on the elastic properties and the deformability of the medium, the response of N2 could be less affected by the hydraulic fracture propagation. In the case of a more compliant medium, a larger part of the deformation will be accommodated by the intact material elastically deforming. Therefore, the stress effect will be less pronounced, and N2 will exhibit a higher normal deformation with a higher calculated flow rate for the isotropic and bimaterial models. N2 stays hydraulically active around 40° when elastic anisotropy is introduced either in the bilayer model or in the transversely isotropic model (black and red lines in Fig. 12e). For the half-plane N1, the curve showing the response of the fracture as a bimaterial interface is always between the curves of the two isotropic material cases (red lines in Fig. 12a, b, c). The shear displacement on N1 is higher for a transversely isotropic material than for an isotropic one. N2 is exhibiting higher shear displacement when a weaker Young's modulus characterizes the layer above the plane (blue and red lines in Fig. 12f). For higher dip angles $> 40°$, the recorded magnitudes vary in the same range approximately.

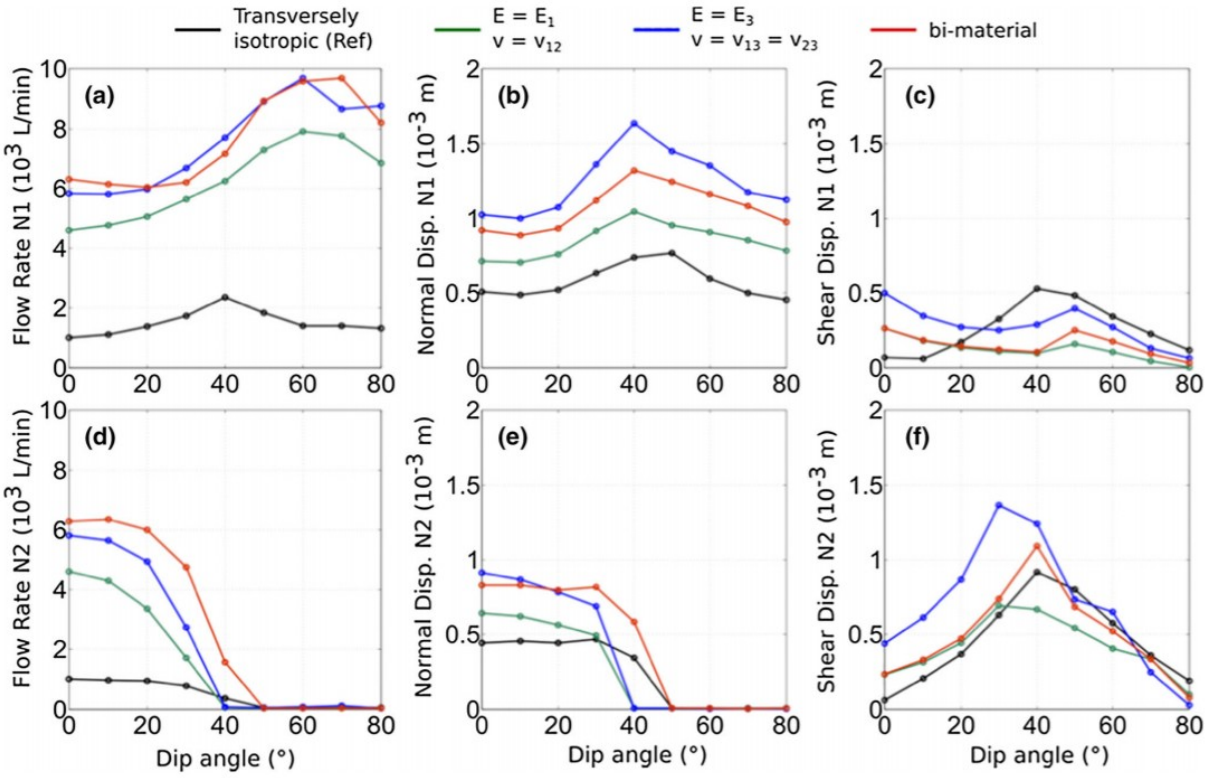

Fig. 12 Variation of flow rate (left column), normal displacement (middle column) and shear displacement (right column) for N1 (top line) and N2 (bottom line) as a function of the elastic properties of the surrounding medium

4 Discussion

In the model described in Sect. 2, the effect of the fracture network geometry was considered. The properties of the fractures were identical and the inter-connectivity was assumed to be high since all fractures were persistent. Nevertheless, the fracture network was not found to be overall stimulated apart from a rather small number of fractures that conducted the fluid promoting preferential flow path at the scale of the network. The effects of the stress field and the orientation of the fractures are highlighted by the results obtained. The fractures that appeared to be hydraulically active in the models presented were just 2 or 3 showing the strong dependency of fracture reactivation on its orientation with respect to the ambient stress field. Even if a high number of fractures were considered, the flow appeared to be always localized as critically stressed fractures are prone to shear failure and dilatancy induced aperture increase (see, e.g., [41]). It was observed that for the present stress conditions, the fractures characterized by a dip angle which is lower than 40° cannot serve as potential fluid paths under a fluid pressure increase in the presence of more favorably oriented fractures.

Comparing with the experimental data, it was not possible to reproduce the observed reversibility of the displacements and the abrupt decrease in the flow rate with the models presented in this section. Modeling results for Test 1 reported in [46] succeeded to represent part of the displacements reversibility. Nevertheless, the geometrical configuration presented was a specific fracture representation that proved to be the best match for the displacements evolution. In an effort to understand the mechanisms behind the in situ response of the stimulated volume, fracture interaction could still be one dominant mechanism. However, reproducing in a numerical model a similar mechanism would require considering a large number of different combinations and scenarios due to the uncertainty regarding the geometry of the network and the fractures' hydromechanical properties.

Apart from the pressure decreasing part of the test, the numerical study presented above can provide some information regarding the in situ properties of the surrounding fractures. Discrepancies between the measured data and the model results suggest that the fractures dipping 20° are characterized by "stronger" mechanical properties than the ones assumed in the modeling that might as well be attributed to the strong cementation present in the fault zone. Modeling of the fractures dipping > 20° showed reasonable agreement with the field data. However, the high calculated flow rate implies that even though the sub-vertical fractures could contribute to the response mechanically, their hydraulic activation is much more limited in situ. It is possible that these structures could be better considered as partially calcified implying a channeling flow regime along their plane as a result of the presence of calcite patches and therefore heterogeneous properties. Indeed, numerical studies on fracture network flow showed that even local heterogeneities along the interconnected

fracture planes can significantly affect the bulk permeability of the network [21].

The sensitivity study performed with the model of two intersecting fractures showed the importance of three parameters, i.e., the stress field, the fracture's orientation with respect to the maximum stress and the intact rock's elastic properties. Based on the numerical results, we observe two distinct responses on the same natural fracture plane showing that even for a simple configuration, the mechanisms of fracture interaction can be quite complex. A natural fracture separated by a fluid-induced or cemented fracture will respond differently on each of its sides. The response depends on the orientation of the plane toward the maximum principal stress and on the angle between the natural and the hydraulic fracture.

The response of the half-plane which is away from the HF (N1) is conditioned by the effective stress variations in the plane, which is in accordance with previous works focusing on the hydraulic–natural fracture interaction [8, 55, 62] and failure and fracture-controlled permeability enhancement in fault zones [16, 25]. Under an isotropic state of stress, and for a range of fracture and rock properties, the half-plane is activated for all possible orientations. When stresses are isotropic, the large fluid absorbed by the NF induces a pressure decrease in the HF, and when there is a high differential stress, shear failure on the NF favoring an increase in σ_3 relative to σ_1 close to the fluid front can stop the fracture reactivation. This result is complementary to other theoretical studies that showed that for high differential stresses and specific angles of approach (probably depending on the friction coefficient) the hydraulic fracture is not crossing the natural fracture but is arrested by shear slippage with no opening and diverting of fluid in the natural fracture [37, 55, 61, 62]. For a medium differential stress, resulting in a stress ratio $\sigma_1/\sigma_3 = 2$ which is similar to the natural stress conditions of the field test ($\sigma_2/\sigma_3 = \sigma_1/\sigma_3 = 2$) described above, the half-plane is reactivated for a dip angle $> 60°$ meaning an angle $< 30°$ with respect to σ_1. This is representative of the response observed in the modeling results of the multi-fracture model of Test 1 in Sect. 2 where only fractures characterized by an orientation of $<$ 40° with respect to σ_2 (which is very close to σ_1) can act as potential fluid paths, while the rest stay almost completely hydraulically inactive.

Considering the half-plane the closest to the HF and a state of stresses close to isotropic, the natural fracture will "easily" absorb the fluid for HF-NF angles $> 50°$. For a slight ~ 2 MPa differential stress, the natural fracture will only experience a purely mechanical shear activation for HF-NF angles $< 50°$. This kind of natural fracture response was not observed in the Test 1 multi-fracture model since the normal deformation of the reactivated planes was limited and part of the fractures formed an angle $\geq 50°$ with the reactivated planes. For higher differential stresses of ~ 20 MPa, shear is triggered on a larger zone affecting the two natural fracture's half-planes.

Referencing to the well-studied fracture interaction and microseismic monitoring during hydraulic fracturing operation for unconventional shale reservoirs, this contrasted shear behavior of the two half-planes shows that both “wet” and “dry” events can be potentially produced on the same stimulated natural fracture. The “dry” events are associated with the response of the plane that is closer to the fluid-driven fracture that exhibits shear deformation and is not related to fluid flowing into the fracture. This is a complementary result to previous works from [43] that showed that stress transfer effects could trigger “dry” events on different fractures not hydraulically connected to the reactivated HF.

The hydraulic fracture in the models is strictly developing along a predefined plane. This can be considered as a strong assumption for newly created fractures since even if the crack would mainly grow along the direction of the maximum stress, direction changes are possible near the interfaces due to interactions between the sheared and dilated fracture branches [34]. In addition, at zero or low differential stresses, variations in material properties tend to become more important than stress orientation in controlling the direction of fracture propagation [8]. Nevertheless, the assumption of a predefined plane of propagation or activation is not very strong if we consider that the fracture is a preexisting plane characterized by a higher cohesion and tensile strength or high fraction of surface contact areas.

The sensitivity analysis results show that the mechanical properties of the natural fracture slightly influence its response to the HF–NF interactions, while the bulk properties of the surrounding material have a significant impact mainly on the magnitudes of the flow rate and displacements of the natural fracture. Indeed, for lower shear stiffness, an increase in the flow rate was observed for N1 and a decrease for N2 at a dip angle equal to 40°. A friction angle of 10° lower than the reference case had the same effect as the shear stiffness on the flow rate of the two half-planes. When anisotropy of the intact rock properties is considered or when the natural fracture is figured as the boundary between two materials of contrasted elastic properties, the flow rate and normal deformation tend to significantly vary, while the shear displacement on the fracture plane remains more or less the same. Anisotropy of the mechanical elastic properties which is a common feature of shales and of many sedimentary rocks is known to influence the in situ stress [1]. Bimaterial interfaces are often encountered in fault zones where slip surfaces develop at the boundary between high elasticity granular and intensely deformed cores and fractured damage zones. Our results are in good accordance with studies showing that contrasted bimaterial properties favor changes in the compressive normal stress and promote slip on the interface between the two materials [11, 57].

5 Conclusions

A hydromechanical model has been set up to simulate an experimental injection test which uses an advanced hydromechanical probe (mHPP). The

model confirmed that considering reasonable property values, very small displacements, i.e., at the dozen micrometers scale, along preexisting discontinuities can dramatically increase the flow rate inside the rock mass at the decameter scale. Thereafter, and based on the hydromechanical properties used to simulate this in situ test, the model has been used to perform a parametric study to identify the key parameters controlling the hydromechanical response of connected fractures. The significant role of both, stress and orientation, was quantified showing that under a differential stress equal to 2 MPa (i.e., for a stress ratio $\sigma_1/\sigma_3 = 2$), fractures forming an angle higher than 40° with the maximum stress (dip angle lower than 50°) cannot be reactivated. The sensitivity analysis carried out with the simple two fractures model showed that contrasted responses can coexist on the same fracture plane but on both sides of the crossing zone, depending on the orientation and size of the natural fracture, on the stress field and on the vicinity to adjacent reactivated planes. A decoupling between the permeability and the mechanical response (i.e., shear displacement) may occur along the natural fracture plane. This decoupling occurs for dip angles higher than 20° under homogeneous stress conditions and for dip angles higher than 60° under a differential stress equal or higher than 2 MPa but lower than 20 MPa.

Thus, the calibrated model shows that the relative orientation of the discontinuities within the stress field is of first order in the hydromechanical behavior of connected fractures. Nevertheless, the elastic properties of the medium can also greatly affect the response of fractures, which exhibit higher normal displacement and flow rate in the case of an isotropic intact material instead of transversely isotropic. Hence, the intact material properties should be well calibrated especially in shale and fault environments, for which anisotropic properties of the fabric can greatly modify the hydromechanical response.

Acknowledgements

The first author would like to thank Total S.A. for funding this research project (contract FR00006163).

References

1.

Amadei B, Savage WZ, Swolfs HS (1987) Gravitational stresses in anisotropic rock masses. Int J Rock Mech Min Sci Geomech Abstr 24(1):5–14

2.

Auradou H, Drazer G, Boschan A, Hulin JP, Koplik J (2006) Flow channeling in a single fracture induced by shear displacement. Geothermics 35(5–6):576–588

3.

Balsamo F, Storti F, Salvini F, Silva AT, Lima CC (2010) Structural and petrophysical evolution of extensional fault zones in low-porosity, poorly lithified sandstones of the Barreiras Formation, NE Brazil. J Struct Geol 32(11):1806–1826

4.

Barton CA, Zoback MD, Moos D (1995) Fluid flow along potentially active faults in crystalline rock. Geology 23(8):683–686

5.

Barton CA, Hickman S, Morin RH, Zoback MD, Finkbeiner T, Sass J, Benoit D (1997) Fracture permeability and its relationship to in situ stress in the Dixie Valley, Nevada, geothermal reservoir

6.

Behnia M, Goshtasbi K, Marji MF, Golshani A (2015) Numerical simulation of interaction between hydraulic and natural fractures in discontinuous media. Acta Geotech 10(4):533–546

7.

Berkowitz B (2002) Characterizing flow and transport in fractured geological media: a review. Adv Water Resour 25(8–12):861–884

8.

Blanton TL (1986, January) Propagation of hydraulically and dynamically induced fractures in naturally fractured reservoirs. In: SPE unconventional gas technology symposium. Society of Petroleum Engineers

9.

Boisson JY, Bertrand L, Heitz JF, Golvan Y (2001) In situ and laboratory investigations of fluid flow through an argillaceous formation at different scales of space and time, Tournemire tunnel, southern France. Hydrogeol J 9(1):108–123

10.

Bossart P (2011) Characteristics of the Opalinus clay at Mont Terri

11.

Cappa F (2011) Influence of hydromechanical heterogeneities of fault zones on earthquake ruptures. Geophys J Int 185:1049–1058

12.

Cappa F, Guglielmi Y, Rutqvist J, Tsang CF, Thoraval A (2006) Hydromechanical modelling of pulse tests that measure fluid pressure and fracture normal displacement at the Coaraze Laboratory site, France. Int J Rock Mech Min Sci 43(7):1062–1082

13.

Cornet FH (2000) Détermination du champ de contrainte au voisinage du laboratoire souterrain de Tournemire. Rapport du Laboratoire de Mécanique des Roches, Département de Sismologie, Institut de Physique du Globe de Paris, Rapport N98N33/0073

14.

Cornet FH (2016) Seismic and aseismic motions generated by fluid injections. Geomech Energy Environ 5:42–54

15.

Cox SF (1995) Faulting processes at high fluid pressures: an example of fault valve behavior from the Wattle Gully Fault, Victoria, Australia. J Geophys Res Solid Earth 100(B7):12841–12859

16.

Cox SF (2010) The application of failure mode diagrams for exploring the roles of fluid pressure and stress states in controlling styles of fracture-controlled permeability enhancement in faults and shear zones. Geofluids 10(1–2):217–233

17.

Cuss RJ, Milodowski A, Harrington JF (2011) Fracture transmissivity as a function of normal and shear stress: first results in Opalinus Clay. Phys Chem Earth Parts A/B/C 36(17–18):1960–1971

18.

Damjanac B, Cundall P (2016) Application of distinct element methods to simulation of hydraulic fracturing in naturally fractured reservoirs. Comput Geotech 71:283–294

19.

De Barros L et al (2016) Fault structure, stress, or pressure control of the seismicity in shale? Insights from a controlled experiment of fluid-induced fault reactivation. J Geophys Res Solid Earth 121:4506–4522. https://doi.org/10.1002/2015JB012633

20.

Dick P, Wittebroodt C, Lefevre M, Courbet C, Matray JM (2013) Estimating hydraulic conductivities in a fractured shale formation from pressure pulse testing and 3D modeling, AGU, Fall Meeting 2013, abstract MR11A-2202

21.

Dreuzy JR, Méheust Y, Pichot G (2012) Influence of fracture scale heterogeneity on the flow properties of three-dimensional discrete fracture networks (DFN). J Geophys Res Solid Earth. https://doi.org/10.1029/2012JB009461

22.

Duboeuf L, De Barros L, Cappa F, Guglielmi Y, Deschamps A, Seguy S (2017) Aseismic motions drive a sparse seismicity during fluid injections into a fractured zone in a carbonate reservoir. J Geophys Res Solid Earth 122(10):8285–8304

23.

Eshiet KII, Sheng Y (2017) The role of rock joint frictional strength in the containment of fracture propagation. Acta Geotech 12(4):897–920

24.

Faleiros AM, da Cruz Campanha GA, Faleiros FM, da Silveira Bello RM (2014) Fluid regimes, fault-valve behavior and formation of gold-quartz veins—the Morro do Ouro mine, Ribeira Belt, Brazil. Ore Geol Rev 56:442–456

25.

Fournier RO (1996) Compressive and tensile failure at high fluid pressure where preexisting fractures have cohesive strength, with application to the San Andreas Fault. J Geophys Res Solid Earth 101(B11):25499–25509

26.

Fu W, Ames BC, Bunger AP, Savitski AA (2016) Impact of partially cemented and non-persistent natural fractures on hydraulic fracture propagation. Rock Mech Rock Eng 49(11):4519–4526

27.

Gentier S, Lamontagne E, Archambault G, Riss J (1997) Anisotropy of flow in a fracture undergoing shear and its relationship to the direction of shearing and injection pressure. Int J Rock Mech Min Sci 34(3–4):94-e1

28.

Guglielmi Y, Cappa F, Lançon H, Janowczyk JB, Rutqvist J, Tsang CF, Wang JSY (2013) ISRM suggested method for step-rate injection method for fracture in situ properties (SIMFIP): using a 3-components borehole deformation sensor. In: The ISRM suggested methods for rock characterization, testing and monitoring: 2007–2014. Springer, Cham, pp 179–186

29.

Guglielmi Y, Cappa F, Avouac JP, Henry P, Elsworth D (2015) Seismicity triggered by fluid injection–induced aseismic slip. Science 348(6240):1224–1226

30.

Guglielmi Y, Elsworth D, Cappa F, Henry P, Gout C, Dick P, Durand J (2015) In situ observations on the coupling between hydraulic diffusivity and displacements during fault reactivation in shales. J Geophys Res Solid Earth 120(11):7729–7748

31.

Gutierrez M, Øino LE, Nygaard R (2000) Stress-dependent permeability of a de-mineralised fracture in shale. Mar Pet Geol 17(8):895–907

32.

Itasca CG (2013) 3DEC-User manual. Itasca ConsultingGroup, Minneapolis

33.

Jeanne P, Rinaldi AP, Rutqvist J, Dobson PF(2015, January) Seismic and aseismic deformations occurring during EGS stimulation at The Geysers: IMPACT on reservoir permeability. In: Proceedings, fourtieth workshop on geothermal reservoir engineering

34.

Jeffrey RG, Zhang X, Thiercelin MJ (2009, January) Hydraulic fracture offsetting in naturally fractures reservoirs: quantifying a long-recognized process. In: SPE hydraulic fracturing technology conference. Society of Petroleum Engineers

35.

Khazaei C, Hazzard J, Chalaturnyk R (2016) Discrete element modeling of stick-slip instability and induced microseismicity. Pure Appl Geophys 173(3):775–794

36.

Khazaei C, Hazzard J, Chalaturnyk R (2016) A discrete element model to link the microseismic energies recorded in caprock to geomechanics. Acta Geotech 11(6):1351–1367

37.

Liu Y, Xiu N, Ding Y, Wang X, Lu Y, Dou J, Yan Y, Liang T (2015) Analysis of multi-factor coupling effect on hydraulic fracture network in shale reservoirs. Nat Gas Ind B 2(2):162–166

38.

Matray JM, Savoye S, Cabrera J (2007) Desaturation and structure relationships around drifts excavated in the well-compacted Tournemire’s argillite (Aveyron, France). Eng Geol 90(1–2):1–16

39.

Matsuki K, Kimura Y, Sakaguchi K, Kizaki A, Giwelli AA (2010) Effect of shear displacement on the hydraulic conductivity of a fracture. Int J Rock Mech Min Sci 47(3):436–449

40.

Maxwell SC (2011) What does microseismic tell us about hydraulic fracture deformation. CSEG Rec 36(8):31–45

41.

Min KB, Rutqvist J, Tsang CF, Jing L (2004) Stress-dependent permeability of fractured rock masses: a numerical study. Int J Rock Mech Min Sci 41(7):1191–1210

42.

Miocic JM, Gilfillan SM, Roberts JJ, Edlmann K, McDermott CI, Haszeldine RS (2016) Controls on CO2 storage security in natural reservoirs and implications for CO2 storage site selection. Int J Greenh Gas Control 51:118–125

43.

Nagel NB, Sanchez-Nagel MA, Zhang F, Garcia X, Lee B (2013) Coupled numerical evaluations of the geomechanical interactions between a hydraulic fracture stimulation and a natural fracture system in shale formations. Rock Mech Rock Eng 46(3):581–609

44.

Newell P, Martinez MJ, Eichhubl P (2017) Impact of layer thickness and well orientation on caprock integrity for geologic carbon storage. J Petrol Sci Eng 155:100–108

45.

Rinaldi AP, Rutqvist J, Cappa F (2014) Geomechanical effects on CO2 leakage through fault zones during large-scale underground injection. Int J Greenh Gas Control 20:117–131

46.

Rivet D, De Barros L, Guglielmi Y, Cappa F, Castilla R, Henry P (2016) Seismic velocity changes associated with aseismic deformations of a fault stimulated by fluid injection. Geophys Res Lett 43(18):9563–9572

47.

Rutledge JT, Phillips WS (2003) Hydraulic stimulation of natural fractures as revealed by induced microearthquakes, Carthage Cotton Valley gas field, east Texas. Geophysics 68(2):441–452

48.

Screaton EJ, Carson B, Lennon GP (1995) Hydrogeologic properties of a thrust fault within the Oregon accretionary prism. J Geophys Res Solid Earth 100(B10):20025–20035

49.

Sibson RH (1989) Earthquake faulting as a structural process. J Struct Geol 11(1–2):1–14

50.

Sibson RH (1996) Structural permeability of fluid-driven fault-fracture meshes. J Struct Geol 18(8):1031–1042

51.

Sibson RH, Robert F, Poulsen KH (1988) High-angle reverse faults, fluid-pressure cycling, and mesothermal gold-quartz deposits. Geology 16(6):551–555

52.

Townend J, Zoback MD (2000) How faulting keeps the crust strong. Geology 28(5):399–402

53.

Tremosa J, Arcos D, Matray JM, Bensenouci F, Gaucher EC, Tournassat C, Hadi J (2012) Geochemical characterization and modelling of the Toarcian/Domerian porewater at the Tournemire underground research laboratory. Appl Geochem 27(7):1417–1431

54.

Van Der Baan M, Eaton D, Dusseault M (2013, May) Microseismic monitoring developments in hydraulic fracture stimulation. In: ISRM international conference for effective and sustainable hydraulic fracturing. international society for rock mechanics

55.

Warpinski NR, Teufel LW (1987) Influence of geologic discontinuities on hydraulic fracture propagation (includes associated papers 17011 and 17074). J Petrol Technol 39(02):209–220

56.

Warpinski NR, Du J, Zimmer U (2012) Measurements of hydraulic-fracture-induced seismicity in gas shales. SPE Prod Oper 27(03):240–252

57.

Weertman J (1980) Unstable slippage across a fault that separates elastic media of different elastic constants. J Geophys Res Solid Earth 85(B3):1455–1461

58.

White JA, Chiaramonte L, Ezzedine S, Foxall W, Hao Y, Ramirez A, McNab W (2014) Geomechanical behavior of the reservoir and caprock system at the In Salah CO_2 storage project. Proc Natl Acad Sci 111(24):8747–8752

59.

Witherspoon PA, Wang JSY, Iwai K, Gale JE (1980) Validity of cubic law for fluid flow in a deformable rock fracture. Water Resour Res 16(6):1016–1024

60.

Yaghoubi A, Zoback M (2012) Hydraulic fracturing modeling using a discrete fracture network in the Barnett Shale. In American Geophysical Union, fall meeting

61.

Zhang B, Ji B, Liu W (2018) The study on mechanics of hydraulic fracture propagation direction in shale and numerical simulation. Geomech Geophys Geo-Energy Geo-Resour 4(2):119–127

62.

Zhou J, Chen M, Jin Y, Zhang GQ (2008) Analysis of fracture propagation behavior and fracture geometry using a tri-axial fracturing system in naturally fractured reservoirs. Int J Rock Mech Min Sci 45(7):1143–1152